

HFNG Flux Measurement by Foil Activation

Jonathan T. Morrell*

University of California, Berkeley - Nuclear Engineering

(Dated: April 19, 2018)

In this experiment we use the foil activation technique to measure the fast neutron flux in the Berkeley High Flux Neutron Generator (HFNG). The irradiation began at 11:53 on 10/23/2017 and ended at 23:31 on 10/23/2017. The peak flux measured was $(1.05 \pm 0.14) \cdot 10^7 \left[\frac{n}{cm^2 s} \right]$ using the following monitor channel(s): $^{58}\text{Ni}(n,p)^{58}\text{Co}$.

I. OVERVIEW

The High-Flux Neutron Generator (HFNG), pictured in Fig. 1 is a DD-fusion neutron source operated by the University of California, Berkeley Nuclear Engineering department, located in Etcheverry Hall. The facility is host to a wide range of users, with applications such as neutron activation analysis, cross-section measurements and geochronology.

DD neutron generators have a number of advantages over research reactors as a sources of neutrons: they are safer, cheaper, easier to build and operate, and the neutron flux spectrum in a neutron generator is nearly mono-energetic, with a well characterized energy-angle correlation. Their principal disadvantage is that the peak flux achievable in a neutron generator is several orders of magnitude lower than in a reactor. As such, the neutron flux is a typical figure of merit for a neutron generator, with the goal of getting as high a flux as possible.

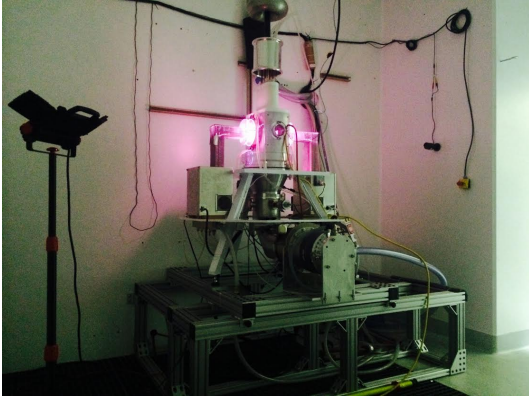


FIG. 1. Photo of the HFNG with both ion sources operating.

A variety of techniques exist for measuring neutron flux. The technique used in this report is that of activation analysis of metal foils. Disk-shaped samples are stamped out of thin metal foils, sealed inside of the HFNG target, and then irradiated for a chosen period

of time. The induced activity is measured by delayed γ -ray emission, counted using a high-purity Germanium (HPGe) detector.

The goal of this report is to give a detailed description of the determination of the neutron flux and energy spectrum in the HFNG, and present the results of this determination for a particular experiment. This report presents the neutron energy and flux for each sample, followed by descriptions of the samples, detector calibrations, Monte-Carlo simulations of the flux spectrum, and a summary of the activation measured in each reaction channel of interest.

I.1. Table of Fluxes

For each sample irradiated in this experiment, the following table summarizes the uncertainty weighted average of the neutron flux measured in each observed reaction channel, as well as the flux-averaged neutron energy and the flux-weighted standard deviation of the neutron energy as determined by Monte Carlo methods. Sample descriptions are provided in the next section.

Sample	Neutron Energy [MeV]	Flux $\left[\frac{n}{cm^2 s} \right]$
1	2.741 ± 0.029	$(1.05 \pm 0.14) \cdot 10^7$
2	2.667 ± 0.044	$(4.81 \pm 0.62) \cdot 10^6$
3	2.615 ± 0.035	$(2.8 \pm 0.39) \cdot 10^6$
4	2.539 ± 0.009	$(3.02 \pm 0.46) \cdot 10^5$
5	2.423 ± 0.017	$(5.26 \pm 0.76) \cdot 10^5$

I.2. Sample Summary

The following table lists the elemental composition and measured mass for each sample irradiated in this experiment, as well as the associated γ -spectrum file(s).

Sample	Element	Mass [g]	γ -Spectrum Filename
1	Ni	0.3275	Ni_NaCl_1.Spe

* jmorrell@berkeley.edu

2	Ni	0.0908	Ni_NaCl_2.Spe
3	Ni	0.09	Ni_NaCl_3.Spe
4	Ni	0.3273	Ni_NaCl_4.Spe
5	Ni	0.3274	Ni_NaCl_5.Spe

The following table lists the radius of each sample disk, as well as the coordinates of the sample inside the HFNG target relative to the origin of the (left side) beam spot. $\Delta\theta$ indicates angle relative to the normal vector of the beam, which should only be non-zero if the sample-holder used was elbows.

Sample	R [mm]	Δx [mm]	Δy [mm]	Δz [mm]	$\Delta\theta$ [°]
1	5.5	0.0	0.0	8.5	0
2	5.5	9.0	8.0	8.5	0
3	5.5	18.0	0.0	8.5	0
4	5.5	36.0	0.0	8.5	0
5	5.5	46.0	0.0	-7.0	90

I.3. Methodology

The general methodology of the thin-foil activation technique proceeds as follows. First the samples are stamped out of metal foils into thin disks, having mass m and number of nuclei

$$n = \frac{w \cdot m \cdot N_A}{M} \quad (1)$$

where w is the isotopic abundance in the sample, M is the molar mass and N_A is Avagadro's number. The sample is usually chosen to have a reaction channel (or multiple channels) with a high cross-section in the DD energy range, about 2-3 MeV, and a half-life comparable to the duration of the irradiation.

Following irradiation, the flux is determined by the ratio of the induced activity to the cross-section, number of nuclei and the fraction of saturation activity F_S .

$$\phi = \frac{A_0}{\sigma n F_S} \quad (2)$$

This represents an average flux, integrated over the area of the sample, the neutron energy spectrum, and over the total irradiation time of the experiment.

If the irradiation takes place in a single, continuous run of time t_i then the saturation fraction will simply be $F_S = (1 - e^{-\lambda t_i})$, where λ is the decay constant of the reaction product. If the irradiation is broken up into

multiple cycles, the saturation fraction will be a recursive function of the cumulative irradiation history.

The induced activity is determined by delayed γ -ray counting using an HPGe detector. If a γ spectrum is counted for a measurement time t_m , beginning some amount of time t_c after the neutron beam was shut off, then the end-of-beam activity measured in a photo-peak having N_c counts will be

$$A_0 = \frac{\lambda N_c}{(1 - e^{-\lambda t_m})e^{-\lambda t_c} I_\gamma \epsilon} \quad (3)$$

where I_γ is the γ emission fraction per decay and ϵ is the detector efficiency at that particular photo-peak energy.

Because the neutron energy spectrum $\psi(E)$ over each sample isn't purely mono-energetic, the cross-section used in the flux calculation should be an averaged cross-section $\bar{\sigma}$ given by

$$\bar{\sigma} = \frac{\int_0^\infty \sigma \psi(E) dE}{\int_0^\infty \psi(E) dE} \quad (4)$$

The flux spectrum used can be determined by Monte Carlo methods, and is discussed later in this report.

II. IRRADIATION HISTORY

The following table lists the start and stop times for each cycle in this experiment, as well as the total number of hours during that interval.

Start	Stop	Total Time [h]
11:53 10/23/2017	23:31 10/23/2017	11.63

This was used to calculate the saturation fraction, F_S discussed previously. The resulting calculation of F_S as a function of the experiment time is plotted below for each reaction channel.

The saturation fraction was calculated in an iterative manner according to the following procedure. For a set of N irradiation cycles with start times S_n and stop times P_n , the saturation factor during a period of irradiation is given by

$$F_n(t_i) = 1 - (1 - I_{n-1} e^{-\lambda(t_i - [P_{n-1} - S_0])}) \quad (5)$$

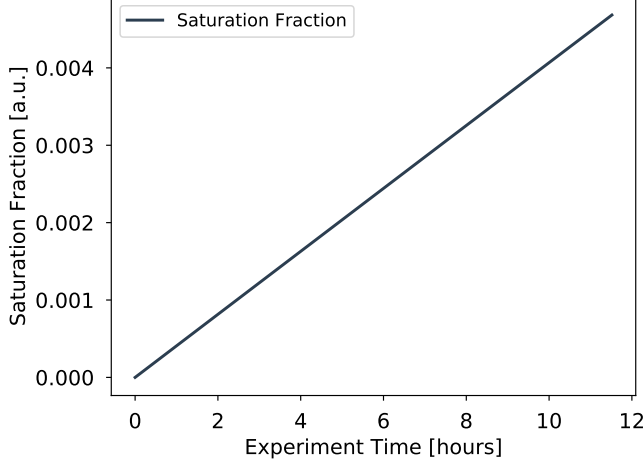


FIG. 2. Saturation fraction, F_S for the ^{58}Co isotope during the irradiation period.

and during a period of decay (between irradiations) is given by

$$F_n(t_d) = I_{n-1}e^{-\lambda(t_d - [P_{n-1} - S_0])} \quad (6)$$

where the constants I_n are recursively determined by

$$I_n = 1 - (1 - I_{n-1}e^{-\lambda(P_n - P_{n-1})})e^{-\lambda(P_n - S_n)} \quad (7)$$

where $I_1 = 0$. The saturation factor used to calculate the flux is simply $F_S = I_N$, i.e. the saturation factor corresponding to the last irradiation cycle.

III. CALIBRATION

The energy and efficiency of the HPGe detector used in this measurement were calibrated using a standard calibration source of known activity (rel. error $<1\%$). Additionally the peaks used in the calibration were used to characterize the resolution of the detector (and associated signal processing units).

A linear calibration of the γ -ray energy E to the MCA channel number N , $E = m \cdot N + b$, was applied, and a plot of the residuals (Fig. 3) shows that this is the correct functional form of the energy calibration, i.e. that there is no quadratic component to the detector response.

A modified 2nd order polynomial was applied for the detector efficiency calibration according to the equation

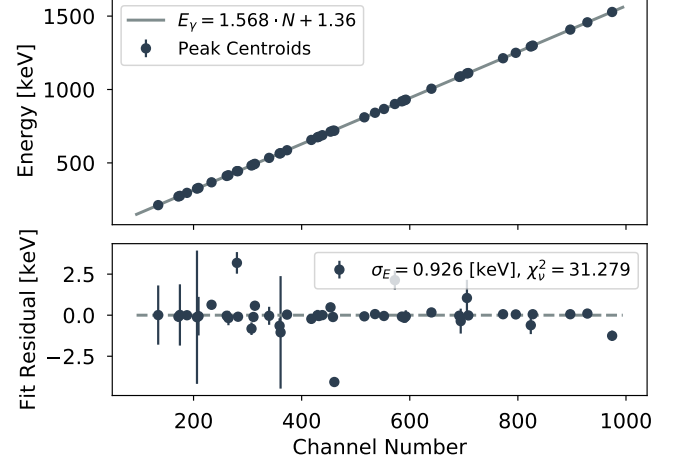


FIG. 3. Linear energy calibration, and plot of the fit residuals.

$$\epsilon(E) = \exp[a \cdot \ln(E)^2 + b \cdot \ln(E) + c] \quad (8)$$

where ϵ is the efficiency and a , b , and c are fitting constants. The resulting fit for the detector efficiency used in this experiment is plotted in figure 4, showing reasonably good agreement.

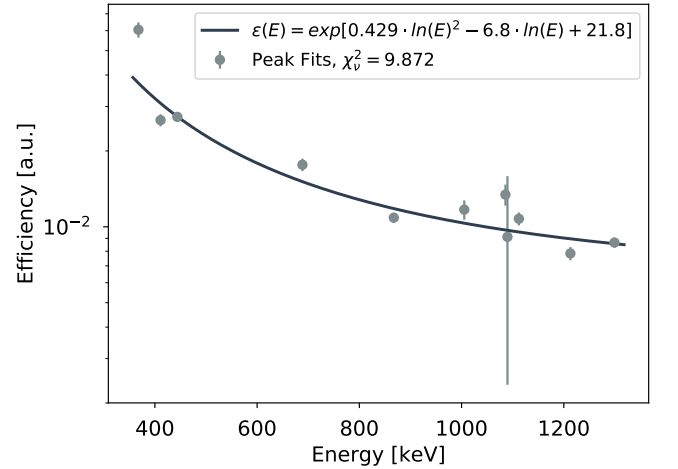


FIG. 4. Detector efficiency calibration, relative to γ emitting efficiency standard of known activity.

The resolution for a HPGe detector should be proportional to the square root of the γ energy, or in terms of the MCA channel number N for a linear calibration

$$\sigma = \delta\sqrt{N} \quad (9)$$

where δ is a proportionality constant, usually a few percent. The fit to equation 9 is plotted in figure 5, below.

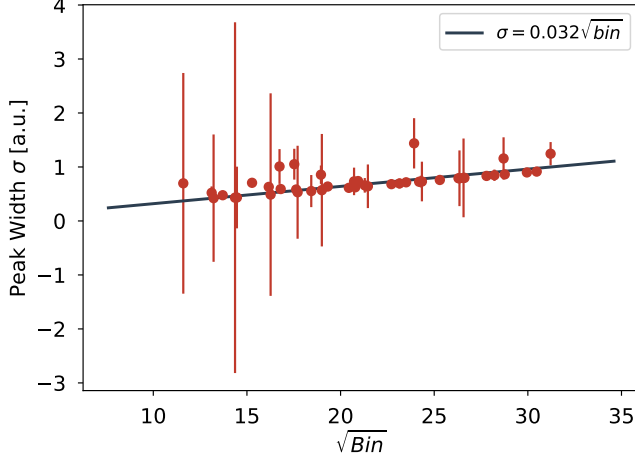


FIG. 5. Detector resolution calibration, and fit to equation 9.

IV. MONITOR FOIL CHARACTERIZATION

In order to choose a value for a tabulated reaction cross-section with which to calculate the average neutron flux on a foil, the neutron energy spectrum must be known either from measurement or calculation. The approach taken in this experiment was to use a Monte Carlo model to calculate this flux spectrum.

In this model, scattering and absorption were treated as negligible as neutrons traverse less than 1 mfp through the HFNG target before reaching the foils. The four physical effects considered in this model were the radial distribution of the neutron beam, the energy-angle correlation of the neutron source, the intensity-angle correlation, and the solid angle.

The flux spectrum for each sample was evaluated using the Monte Carlo method, a numerical technique for evaluating definite integrals. The flux spectrum in a sample can be seen as an integral of a source distribution $S(\vec{r}, E, \hat{\Omega})$ over space d^3r and solid angle $d\hat{\Omega}$. This can be rewritten as a Monte Carlo sum using the definition of the integral

$$\begin{aligned}\bar{\phi}(E) &= \int \int S(\vec{r}, E, \hat{\Omega}) d^3r d\hat{\Omega} \\ &= \int \int \phi_0 \frac{n(\vec{r})\delta(\hat{\Omega} - \hat{\Omega}_{sample})R(\theta(E))}{|\vec{r} - r|^2} d^3r d\hat{\Omega} \\ &= \frac{1}{N} \sum_{n=1}^N \phi_0 \frac{R(\theta(E_n))\delta_{r\theta}}{(\Delta r_n)^2} = \phi_0 \sum_{n=1}^N \frac{R(\theta(E_n))\delta_{r\theta}}{(\Delta r_n)^2}\end{aligned}$$

where $n(\vec{r})$ is PDF for source (e.g. Gaussian) and $\delta_{r\theta}$ constrains neutron rays to source-sample paths.

The energy angle correlation used in this method is well-characterized, and is described using a four term polynomial

$$E_n(\theta) = A_0 + \sum_{n=1}^3 A_n \cos^n(\theta) \quad (10)$$

where the coefficients A_n are given by the following table.

A_n	100 keV	200 keV
A_0	2.4674	2.47685
A_1	0.30083	0.39111
A_2	0.01368	0.04098
A_3	0.0	0.02957

These coefficients can be interpolated based on the exact D^+ beam energy determined by the voltage on the cathode. Figure 6 plots this correlation over all outgoing neutron angles, although most samples are at low angles.

A similar, 6 term polynomial can be used to describe the relative intensity, or yield, as a function of angle:

$$\frac{R(\theta)}{R(90^\circ)} = 1 + \sum_{n=1}^5 A_n \cos^n(\theta) \quad (11)$$

where $\frac{R(\theta)}{R(90^\circ)}$ is the ratio of emission at angle θ to 90° . The polynomial coefficients A_n are listed in the following table.

A_n	100 keV	200 keV
A_1	0.01741	-0.03149
A_2	0.88746	1.11225
A_3	0.22497	0.38659
A_4	0.08183	0.26676
A_5	0.37225	0.11518

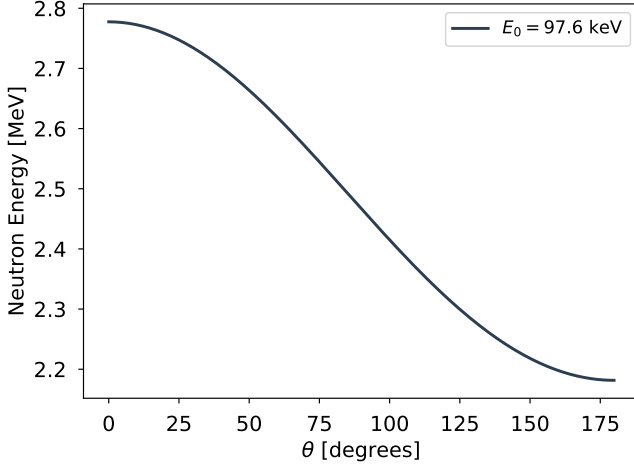


FIG. 6. DD fusion neutron emission energy angle correlation for the incident deuteron beam energy used in this experiment.

A plot of equation 11 using the coefficients for the incident beam energy set in this experiment is shown in Figure 7.

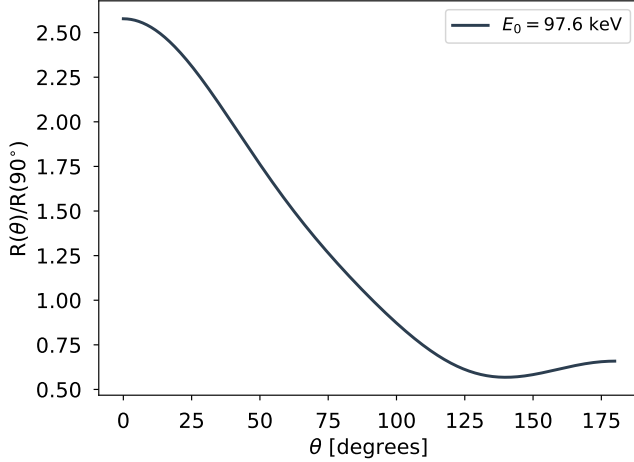


FIG. 7. DD fusion neutron emission intensity angle correlation for the incident deuteron beam energy used in this experiment.

Coordinates for the neutron rays were randomly generated from a Gaussian distribution with a radius determined by measurements of the beam-spot size on the target. The sample coordinates were generated from a uniform distribution, but the correct spatial profile was achieved by weighting each tally according to the intensity-angle correlation and the distance squared.

Using these randomly generated coordinates, the emission angle can be calculated according to the definition of a dot-product of two vectors

$$\theta = \arccos\left(\frac{\vec{r}_1 \cdot \vec{r}_2}{|\vec{r}_1||\vec{r}_2|}\right) \quad (12)$$

where \vec{r}_1 is the normal vector to the neutron beam, and \vec{r}_2 is the vector connecting the source and sample coordinates. An example in 2D is shown in Figure 8, where $\vec{r}_1 = \langle 0, \Delta z \rangle$ and $\vec{r}_2 = \langle \Delta x, \Delta z \rangle$.

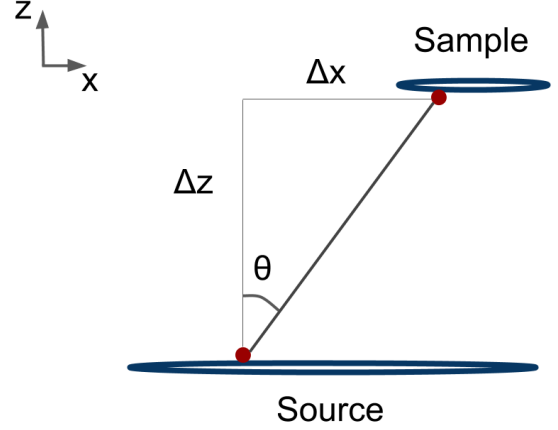


FIG. 8. Schematic showing a 2D example of the randomly selected source and sample points that define the neutron ray. The energy is determined by the angle, and the flux tally is weighted by the angular-intensity correlation and the square of the path length of the neutron ray.

This method was applied for each sample using the geometry as described in the sample summary section, using 100,000 weighted flux tallies. Plots of the resulting calculated flux spectra can be seen below, along with the mean energy and $\pm 1\sigma_E$ of the distribution.

This spectrum was then used to calculate an average cross-section for each reaction channel according to equation 4. The tabulated cross-sections used in this calculation were interpolated from the most recent EXFOR database. Plots of these data, as well as the interpolated values and $\pm 1\sigma_{interp}$ can be seen in the figures below.

The resulting flux-averaged cross-section values for each sample and reaction channel are listed in the following table.

Sample	Reaction	Energy [MeV]	Cross-Section [mb]
1	$^{58}\text{Ni}(n,p)^{58}\text{Co}$	2.741 ± 0.029	149.7 ± 10.8
2	$^{58}\text{Ni}(n,p)^{58}\text{Co}$	2.667 ± 0.044	137.2 ± 9.7
3	$^{58}\text{Ni}(n,p)^{58}\text{Co}$	2.615 ± 0.035	128.8 ± 9.5
4	$^{58}\text{Ni}(n,p)^{58}\text{Co}$	2.539 ± 0.009	116.4 ± 9.7
5	$^{58}\text{Ni}(n,p)^{58}\text{Co}$	2.423 ± 0.017	99.6 ± 7.6

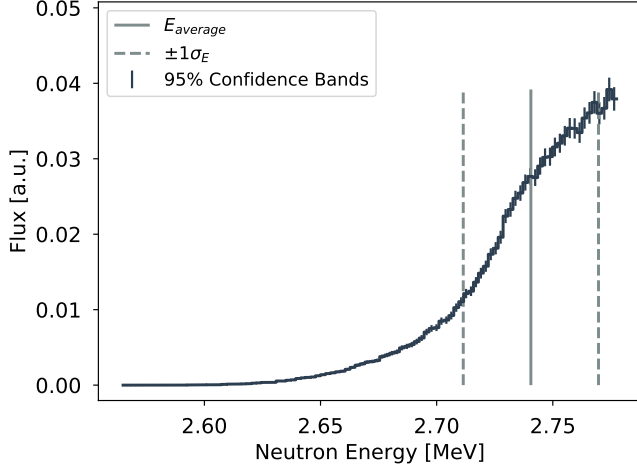


FIG. 9. Energy spectrum, mean and $\pm 1\sigma_E$ for sample 1 calculated by Monte Carlo method.

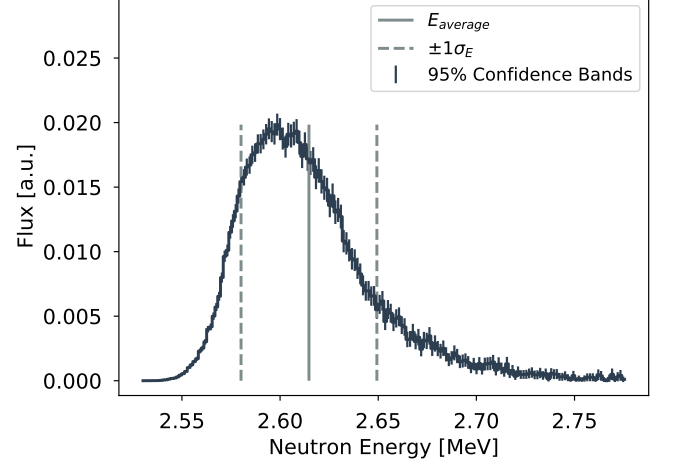


FIG. 11. Energy spectrum, mean and $\pm 1\sigma_E$ for sample 3 calculated by Monte Carlo method.

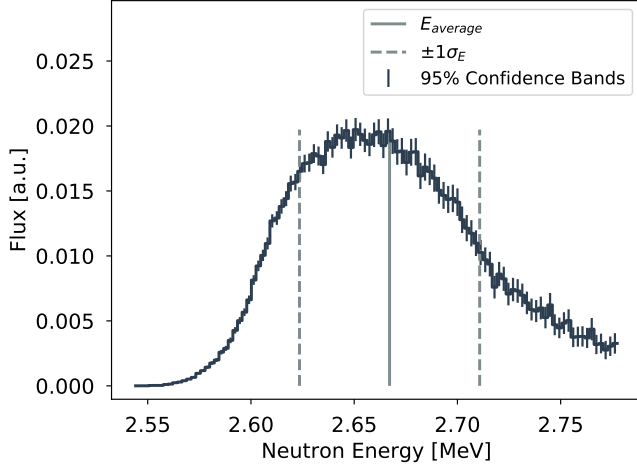


FIG. 10. Energy spectrum, mean and $\pm 1\sigma_E$ for sample 2 calculated by Monte Carlo method.

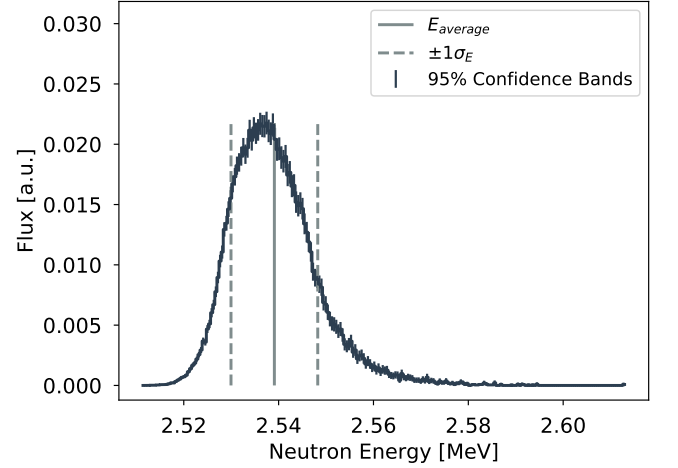


FIG. 12. Energy spectrum, mean and $\pm 1\sigma_E$ for sample 4 calculated by Monte Carlo method.

V. DECAY CURVES

For a single photopeak having N_c counts observed with efficiency ϵ from a radioactive nucleus with decay constant λ and intensity I_γ , equation 3 can be used to calculate the end-of-beam activity for a given isotope. However, if multiple photopeaks are to be used in the calculation the activity at some cooling time t_c after the end-of-beam, the activity in a photopeak can be calculated by

$$A(t_c) = \frac{\lambda N_c}{(1 - e^{-\lambda t_m}) I_\gamma \epsilon} \quad (13)$$

where t_m is the measurement time. The end-of-beam activity A_0 can then be calculated by a Levenberg Marquardt fit to the equation

$$A(t_c) = A_0 e^{-\lambda t_c} \quad (14)$$

The photopeak activities and exponential fits for each reaction channel of interest are plotted in the figures below.

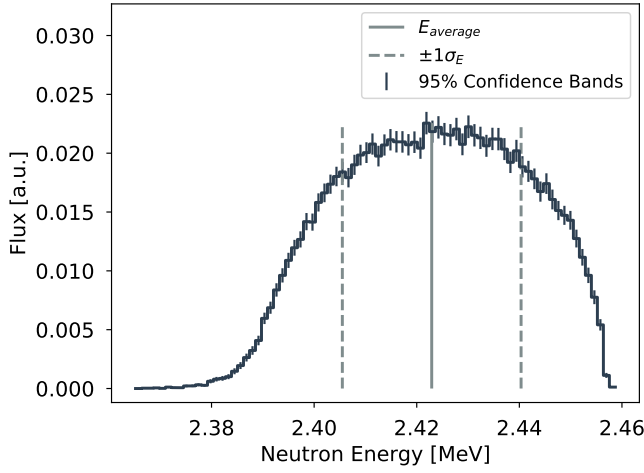


FIG. 13. Energy spectrum, mean and $\pm 1\sigma_E$ for sample 5 calculated by Monte Carlo method.

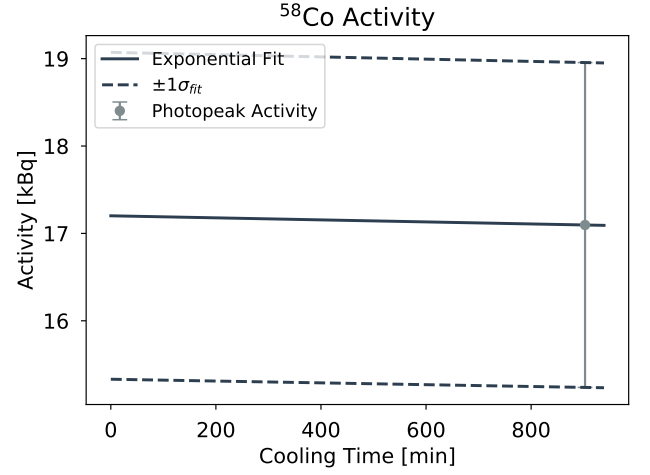


FIG. 15. Exponential fit to the peak activities of ^{58}Co measured in Sample 0.

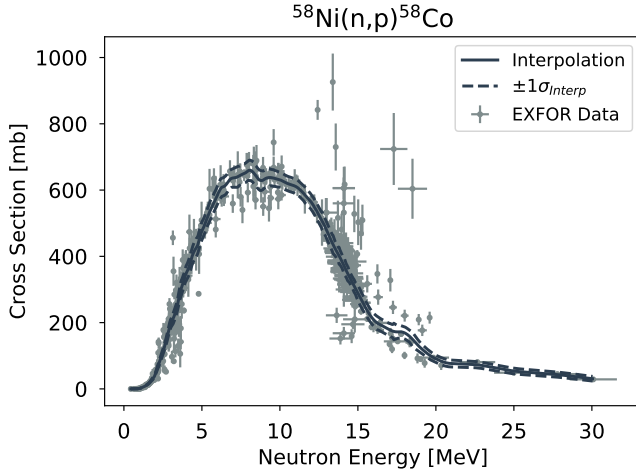


FIG. 14. $^{58}\text{Ni}(n,p)^{58}\text{Co}$ cross section. Data points are from EXFOR, solid/dashed lines are interpolated and $\pm 1\sigma$ values.

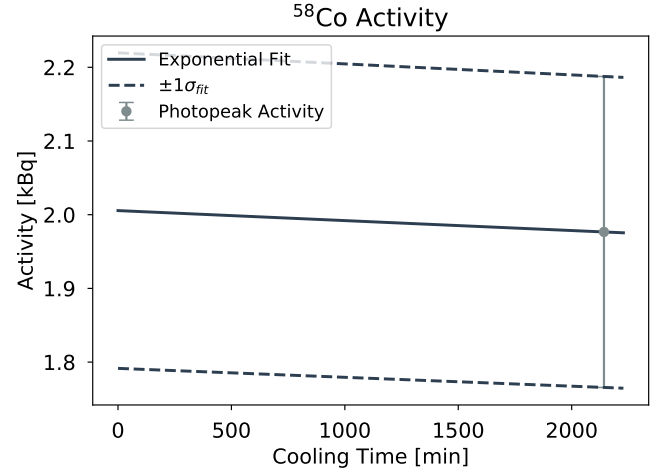


FIG. 16. Exponential fit to the peak activities of ^{58}Co measured in Sample 1.

VI. RESULTS

Finally, the masses of each sample were determined by a high-precision digital scale, and using the values of σ , A_0 and F_s discussed previously the flux values for each reaction channel in each sample were calculated using equation 2 and are listed in the following table.

Sample	Reaction	Energy [MeV]	Flux [$\frac{n}{cm^2 s}$]
1	$^{58}\text{Ni}(n,p)^{58}\text{Co}$	2.741 ± 0.029	$(1.05 \pm 0.14) \cdot 10^7$
2	$^{58}\text{Ni}(n,p)^{58}\text{Co}$	2.667 ± 0.044	$(4.81 \pm 0.62) \cdot 10^6$
3	$^{58}\text{Ni}(n,p)^{58}\text{Co}$	2.615 ± 0.035	$(2.8 \pm 0.39) \cdot 10^6$
4	$^{58}\text{Ni}(n,p)^{58}\text{Co}$	2.539 ± 0.009	$(3.02 \pm 0.46) \cdot 10^5$

$$5 \quad ^{58}\text{Ni}(n,p)^{58}\text{Co} \quad 2.423 \pm 0.017 \quad (5.26 \pm 0.76) \cdot 10^5$$

The uncertainty weighted average of the flux determined by each reaction channel was calculated for each sample, giving the flux values tabulated at the beginning of this report.

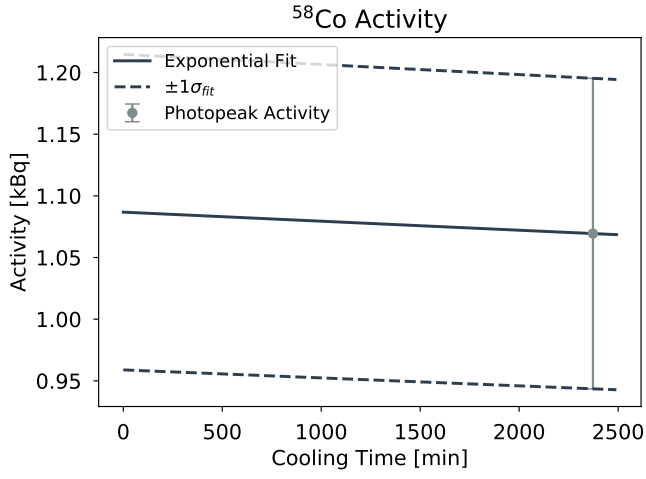


FIG. 17. Exponential fit to the peak activities of ^{58}Co measured in Sample 2.

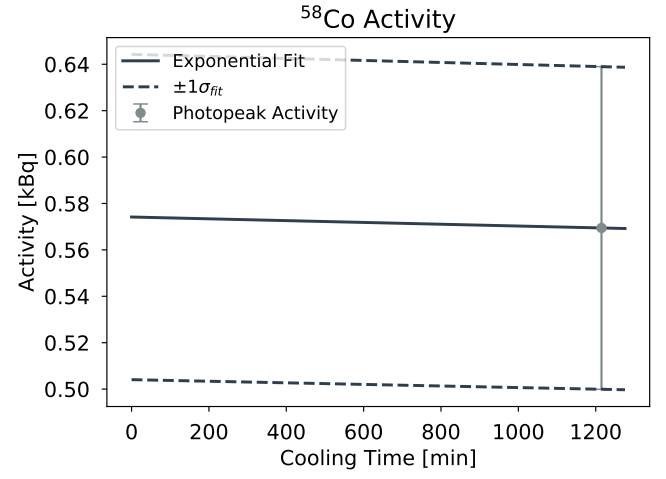


FIG. 19. Exponential fit to the peak activities of ^{58}Co measured in Sample 4.

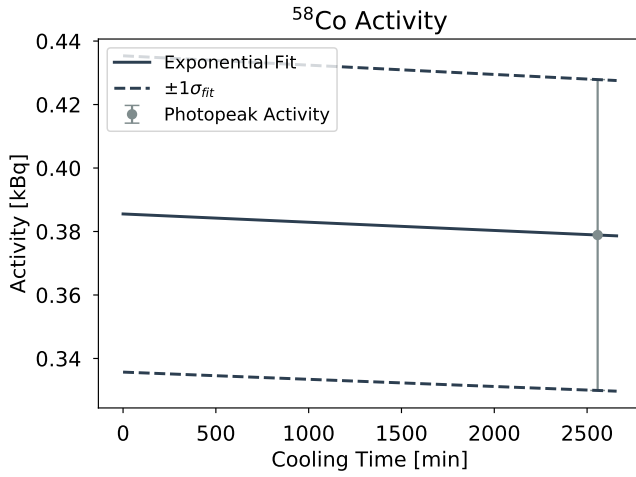


FIG. 18. Exponential fit to the peak activities of ^{58}Co measured in Sample 3.

Appendix A: Peak Fits

The detector energy and efficiency calibration, as well as the induced activity in each sample, was ultimately determined by peak fitting to the individual spectra. Energy centroids and relative intensities were constrained with some uncertainty by the decay data given by the National Nuclear Data Center (NNDC). Each peak was fit with a skewed Gaussian function on top of a linear background. Knoll recommends this as the functional form of a photopeak in an HPGe spectrum because localized charge trapping in the Ge crystal will lead to "tailing" on the low-energy side of the peak. The complete functional form of the peak fit, $F(i)$, as a function of channel number i is as follows.

The "background" under each photopeak, which could be due to actual background radiation or Compton scattering, was given a linear form:

$$F_{bg}(i) = m \cdot i + b \quad (A1)$$

This is purely heuristic but is accurate in most cases because the background tends to be slowly varying over the energy range of one photopeak. The resolution function for HPGe detectors is Gaussian, which means that the convolution of a photopeak (which can be assumed to be a delta function) with the resolution function simply gives a Gaussian peak shape:

$$F_{gauss}(i) = A \cdot \exp\left(-\frac{(i - \mu)^2}{2\sigma^2}\right) \quad (A2)$$

where A is the height of the peak, μ is the mean or centroid and σ is the standard deviation, sometimes called the width of the peak.

The low energy tailing in an ideal detector is characterized by an exponential with argument $\frac{i - \mu}{\beta}$, where β is a width parameter. Convolution of this exponential with a Gaussian resolution function gives a skewed Gaussian:

$$F_{skew}(i) = B \cdot \exp\left(\frac{i - \mu}{\beta}\right) \operatorname{erfc}\left(\frac{i - \mu}{\sqrt{2}\sigma} + \frac{\sigma}{\sqrt{2}\beta}\right) \quad (A3)$$

where B is the height of the skewed Gaussian. In general, B is prportional to A , and β is proportional to σ . We will take advantage of this fact to better constrain our peak fits, as the number of parameters is already somewhat large. Re-configuring the parameters B and β as $B = R \cdot A$, $\beta = \alpha \cdot \sigma$ means the parameters characterizing the skewed Gaussian will only have small variations between peaks and can be fit with much tighter bounds (i.e. faster). For this experiment these skewed Gaussians were found to be approximately parameterized by $R \approx 0.2$ and $\alpha \approx 0.8$.

Finally, the complete equation for individual photopeaks is given by:

$$F_{peak}(i) = m \cdot i + b + A \cdot \left[\exp\left(-\frac{(i - \mu)^2}{2\sigma^2}\right) + R \cdot \exp\left(\frac{i - \mu}{\alpha\sigma}\right) \operatorname{erfc}\left(\frac{i - \mu}{\sqrt{2}\sigma} + \frac{1}{\sqrt{2}\alpha}\right) \right] \quad (A4)$$

Below are plots of the γ -ray spectra for the samples and calibration sources, with photo-peak fits superimposed on the spectrum.

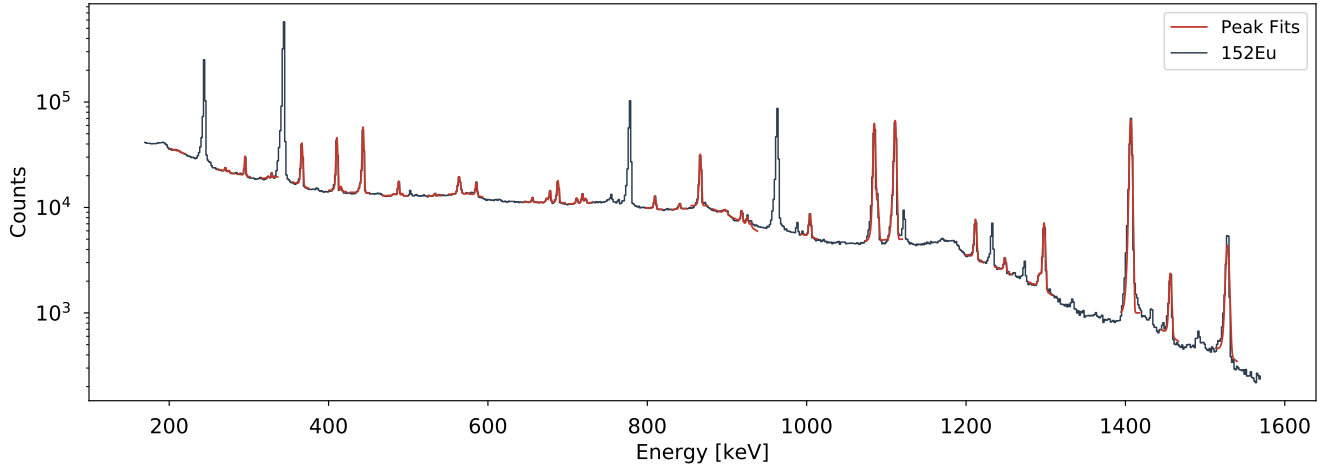


FIG. 20. γ -ray energy spectrum and peak fits in 152Eu.Spe

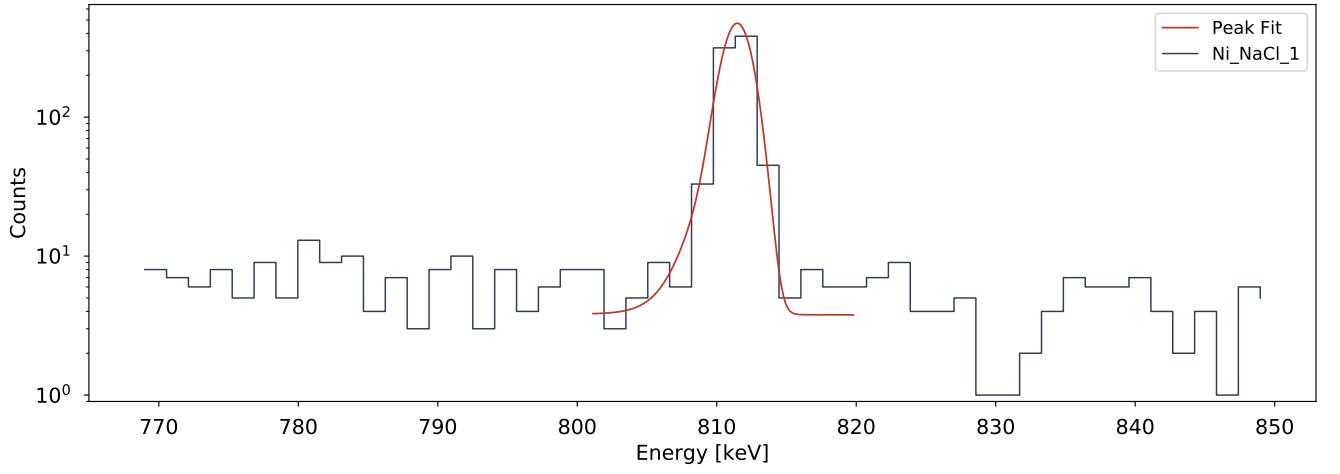


FIG. 21. γ -ray energy spectrum and peak fits in Ni_NaCl_1.Spe

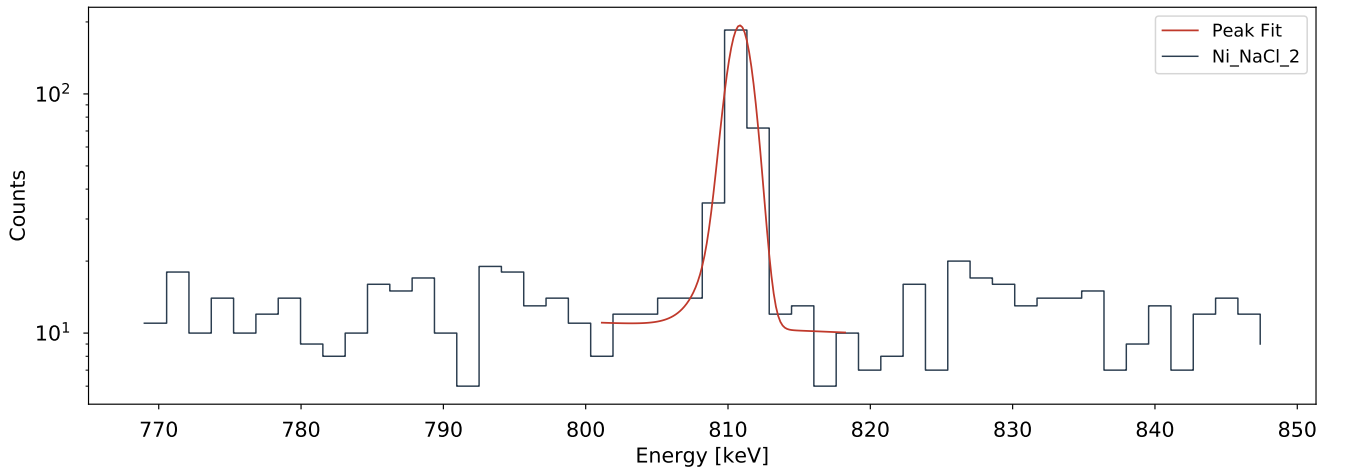
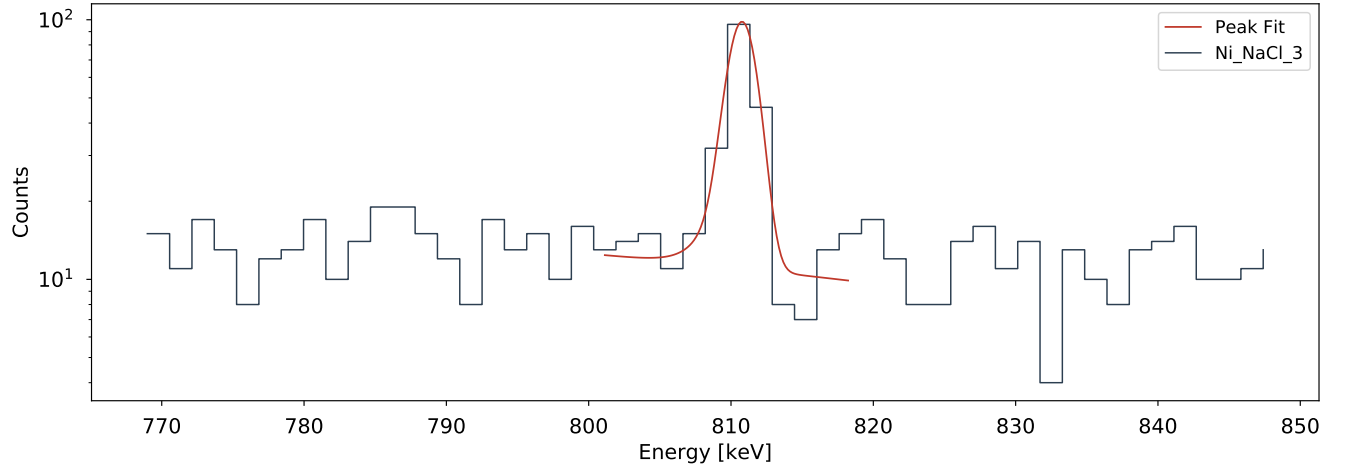
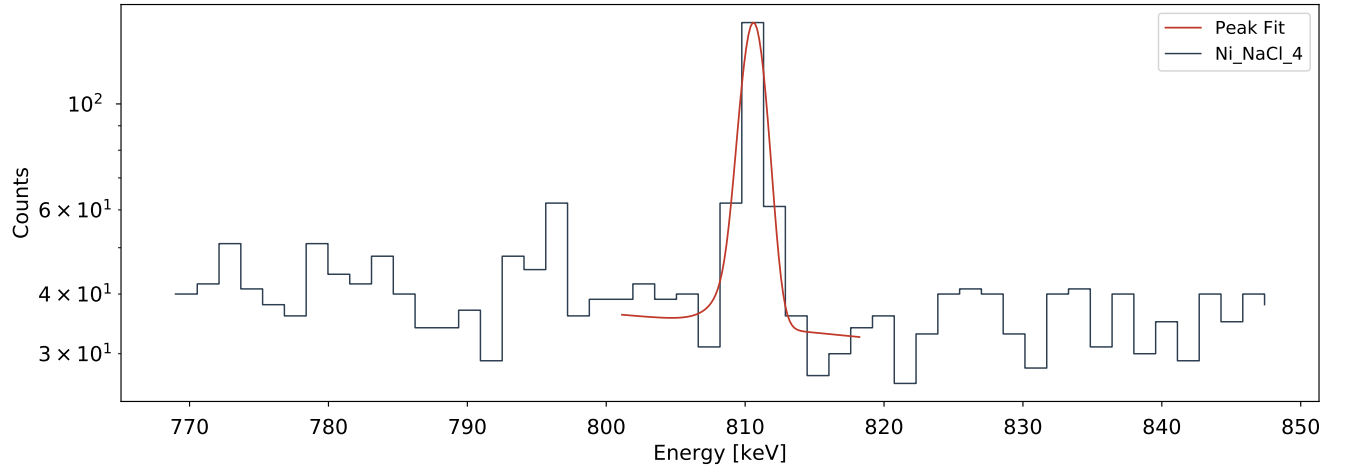
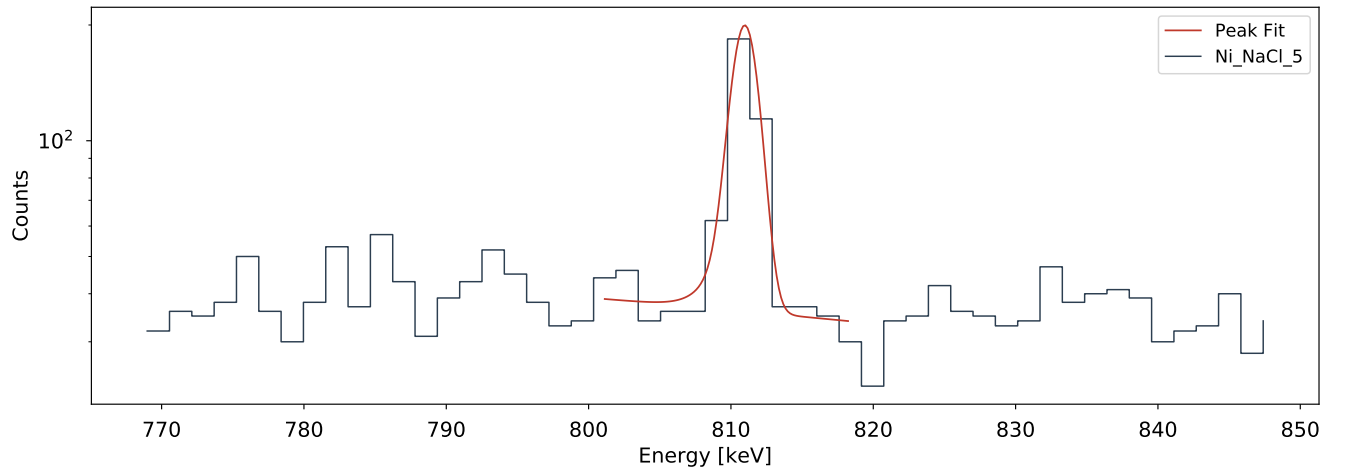


FIG. 22. γ -ray energy spectrum and peak fits in Ni_NaCl_2.Spe

FIG. 23. γ -ray energy spectrum and peak fits in Ni_NaCl_3.SpeFIG. 24. γ -ray energy spectrum and peak fits in Ni_NaCl_4.SpeFIG. 25. γ -ray energy spectrum and peak fits in Ni_NaCl_5.Spe

Appendix B: Table of Peaks

The following table lists the results of the skewed Gaussian peak fits plotted above. Energy and I_γ are NNDC values, counts and χ_ν^2 come from the fits.

Filename	Isotope	γ Energy [keV]	I_γ	Counts	χ_ν^2
152Eu.Spe	¹⁵² Eu	212.43	0.0207±0.0207	1410±4694	9.2
152Eu.Spe	¹⁵² Eu	271.08	0.0715±0.0715	2574±731	2.3
152Eu.Spe	¹⁵² Eu	275.42	0.0346±0.0346	1014±3926	2.3
152Eu.Spe	¹⁵² Eu	295.9387	0.44±0.44	13529±1943	7.2
152Eu.Spe	¹⁵² Eu	324.83	0.0681±0.0681	886±9580	87.5
152Eu.Spe	¹⁵² Eu	329.41	0.1213±0.1213	2501±4173	87.5
152Eu.Spe	¹⁵² Eu	367.7891	0.859±0.859	46955±3266	21.2
152Eu.Spe	¹⁵² Eu	411.1165	2.237±2.237	53545±2951	27.0
152Eu.Spe	¹⁵² Eu	416.02	0.1088±0.1088	2150±11305	27.0
152Eu.Spe	¹⁵² Eu	444.01	0.298±0.298	6139±2227	7.5
152Eu.Spe	¹⁵² Eu	443.9606	2.827±2.827	69713±2200	7.5
152Eu.Spe	¹⁵² Eu	482.33	0.0247±0.0247	1546±521	1.2
152Eu.Spe	¹⁵² Eu	488.6792	0.414±0.414	7669±641	1.2
152Eu.Spe	¹⁵² Eu	493.54	0.0303±0.0303	1003±2065	1.2
152Eu.Spe	¹⁵² Eu	534.25	0.041±0.041	912±603	3.0
152Eu.Spe	¹⁵² Eu	563.986	0.494±0.494	13978±3089	2.8
152Eu.Spe	¹⁵² Eu	566.438	0.131±0.131	1076±2655	2.8
152Eu.Spe	¹⁵² Eu	586.2648	0.455±0.455	7563±1181	9.7
152Eu.Spe	¹⁵² Eu	656.489	0.1441±0.1441	2006±299	3.5
152Eu.Spe	¹⁵² Eu	674.64	0.169±0.169	2081±879	3.5
152Eu.Spe	¹⁵² Eu	678.623	0.473±0.473	5587±626	3.5
152Eu.Spe	¹⁵² Eu	688.67	0.856±0.856	13637±780	3.5
152Eu.Spe	¹⁵² Eu	712.83	0.0955±0.0955	2512±616	1.2
152Eu.Spe	¹⁵² Eu	719.346	0.25±0.25	4229±624	1.2
152Eu.Spe	¹⁵² Eu	719.36	0.095±0.095	2050±1435	1.2
152Eu.Spe	¹⁵² Eu	810.451	0.317±0.317	5656±299	0.8
152Eu.Spe	¹⁵² Eu	841.574	0.168±0.168	2284±377	1.1
152Eu.Spe	¹⁵² Eu	867.38	4.23±4.23	41538±1931	26.8
152Eu.Spe	¹⁵² Eu	901.19	0.0854±0.0854	3583±1412	19.7
152Eu.Spe	¹⁵² Eu	919.337	0.419±0.419	4070±553	19.7
152Eu.Spe	¹⁵² Eu	926.31	0.272±0.272	2503±463	19.7
152Eu.Spe	¹⁵² Eu	930.59	0.0729±0.0729	1102±644	19.7
152Eu.Spe	¹⁵² Eu	1005.27	0.659±0.659	6967±611	6.5
152Eu.Spe	¹⁵² Eu	1085.837	10.11±10.11	122566±11773	235.4
152Eu.Spe	¹⁵² Eu	1089.737	1.734±1.734	14293±10592	235.4
152Eu.Spe	¹⁵² Eu	1109.18	0.189±0.189	7857±7662	235.4
152Eu.Spe	¹⁵² Eu	1112.076	13.67±13.67	132925±7827	235.4
152Eu.Spe	¹⁵² Eu	1212.948	1.415±1.415	10023±604	6.4
152Eu.Spe	¹⁵² Eu	1249.94	0.187±0.187	1907±303	2.4
152Eu.Spe	¹⁵² Eu	1292.78	0.101±0.101	1725±698	6.8
152Eu.Spe	¹⁵² Eu	1299.142	1.633±1.633	12776±583	6.8
152Eu.Spe	¹⁵² Eu	1408.013	20.87±20.87	161274±8302	499.4
152Eu.Spe	¹⁵² Eu	1457.643	0.497±0.497	4354±498	17.4

152Eu.Spe	¹⁵² Eu	1528.1	0.279±0.279	13343±2920	127.4
Ni_NaCl_1.Spe	⁵⁸ Co	810.7593	99.45±9.945	773±33	2.2
Ni_NaCl_2.Spe	⁵⁸ Co	810.7593	99.45±9.945	268±10	0.9
Ni_NaCl_3.Spe	⁵⁸ Co	810.7593	99.45±9.945	145±9	0.8
Ni_NaCl_4.Spe	⁵⁸ Co	810.7593	99.45±9.945	171±14	0.9
Ni_NaCl_5.Spe	⁵⁸ Co	810.7593	99.45±9.945	257±18	0.5